Neutron absolute and total cross section difference measurements in the mass-140 region

H. S. Camarda
The Pennsylvania State University, Delaware County Campus, Media, Pennsylvania 19063
and University of California, Lawrence Livermore National Laboratory, Livermore, California 94550

T. W. Phillips and R. M. White
University of California, Lawrence Livermore National Laboratory, Livermore, California 94550
(Received 23 January 1984)

We have used a 100-MeV electron linac and neutron time-of-flight facility to measure precise neutron total cross sections in the mass-140 region for incident neutron energies of 3–60 MeV. We measured the absolute neutron total cross section of ^{140}Ce and the total cross section differences of ^{139}La–^{140}Ce, ^{141}Pr–^{140}Ce, and ^{142}Ce–^{140}Ce. These cross section differences oscillate with energy. Optical model calculations have been performed which fit the ^{140}Ce total cross section well over the 3–60 MeV energy region. The ^{139}La–^{140}Ce and ^{141}Pr–^{140}Ce difference data were satisfactorily fit by small changes in the geometrical parameters of the potential. The ^{142}Ce–^{140}Ce data could not be fit by small changes in the geometry of the potential and we found that the changes required to achieve a satisfactory fit suggest that ^{142}Ce is either nonspherical or more easily deformed than ^{140}Ce. Using our final optical model parameters we calculated $\delta\langle r^2\rangle = {}^{A}\langle r^2\rangle - {}^{140}\langle r^2\rangle$ for the real part of the potential. The ^{139}La–^{140}Ce and ^{141}Pr–^{140}Ce optical model values of $\delta\langle r^2\rangle$ were in agreement with corresponding $\delta\langle r^2\rangle_q$ values calculated using muonic x-ray data. The value for ^{142}Ce–^{140}Ce was not.

I. INTRODUCTION

Precise neutron total cross section measurements covering a wide range of mass number A and neutron energies from a few MeV to 100 MeV are surprisingly sparse. One reason for this is the lack of intense white neutron sources above 10 or 20 MeV. Much work has been done below 15 MeV where neutrons of sufficient intensity are available from charged particle induced reactions and where white source neutrons are generated using the electron beams of linear accelerators. Some years ago Glasgow and Foster[1] carried out a comprehensive series of neutron total cross section measurements on almost 100 elements between hydrogen and plutonium for neutron energies between 1 and 15 MeV. The spherical optical model calculations they performed indicated that near closed shell nuclei the data could be fit reasonably well. However, between closed shells the fits were unsatisfactory, and a model which includes the effects of nuclear deformation should be used. The measurements of Glasgow and Foster were not of sufficient accuracy to probe subtle differences between neighboring nuclei. In the past several years a few highly precise measurements have been reported on a series of separated isotopes, most of which have permanent deformations, for neutron energies ≤ 15 MeV.[2,3] Optical model analyses have been performed with some success to determine the deformation parameters of these nuclei.

We have completed a series of measurements of neutron absolute and total cross section differences in the mass-140 region for incident neutron energies of 3–60 MeV. The purpose of this investigation has been twofold: (1) to determine the precision and the "maximum" energy with which cross section differences could be measured using the Lawrence Livermore National Laboratory (LLNL) electron linear accelerator and time-of-flight (TOF) facility, and (2) to examine how well an optical model calculation could fit the data and reveal differences between neighboring nuclei. To this end we carried out an absolute total cross section measurement on ^{140}Ce and total cross section difference measurements on ^{139}La–^{140}Ce, ^{141}Pr–^{140}Ce, and ^{142}Ce–^{140}Ce. Except for ^{142}Ce, all these nuclei have a closed neutron shell ($N=82$) and are expected to have a spherical shape.

A simple picture of why the neutron total cross section is sensitive to the interaction strength and range of the optical potential was presented by Peterson.[4] For neutron total cross sections, σ_T vs E is not a monotonically decreasing function of energy but instead exhibits broad positive and negative deviations from some smoothly decreasing function. These broad deviations are the result of constructive and destructive interferences between neutron waves which diffract around and pass through the nucleus. The deviations depend on the range, strength, and shape of the optical potential; for example, a stronger imaginary part of the potential will dampen the deviations as will greater surface diffuseness. Thus these deviations give the total cross section sensitivity to the details of the neutron-nucleus interaction. To first order, the changes in σ_T from one nucleus to the next should be gradual and should be represented by an optical potential with a few slowly varying parameters. Any sudden changes would most likely represent nuclear structure effects peculiar to that nucleus.

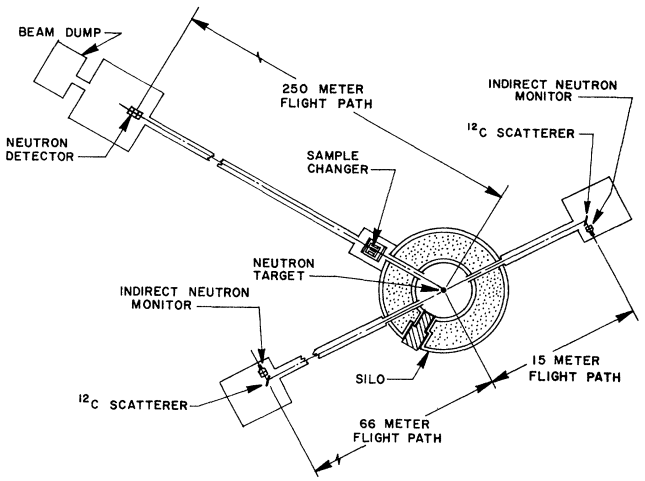

FIG. 1. Schematic view of the above-ground neutron time-of-flight facility. The total cross section measurements were carried out using the 250-m flight path. The 15- and 66-m flight paths were used to monitor the neutron beam.

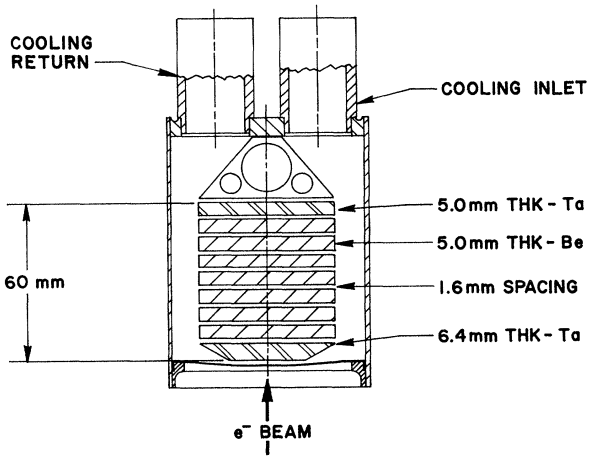

FIG. 2. The Ta-Be neutron producing target in which the electron beam strikes the first tantalum plate converting much of its energy into bremsstralung radiation which subsequently interacts with the Be plates producing neutrons via the (γ,n) reaction.

II. EXPERIMENTAL DETAILS

A. Time-of-flight facility

The experiment was performed using the LLNL electron linear accelerator (located underground) to produce a white neutron source and the TOF technique to determine neutron energies. An electron beam with an energy of 110 MeV was transported above ground where it struck a water-cooled neutron-producing target which was viewed by evacuated flight paths of lengths 15, 66, and 250 m (see Fig. 1). The neutron detector for these measurements was located at the end of the 250-m flight path. The 15- and 66-m flight paths were used to monitor the neutron flux. The accelerator was operated at 1440 pulses per second with a 12-nsec beam-pulse width and an average electron current on target of 55 μA. Using a nonintercepting electron beam position monitor,[5] we were able within a given experimental run to ensure that the electron beam struck the same part of the neutron target to within 1 mm. This helped to ensure run-to-run stability and decreased the normalization errors.

B. Neutron targets

Our initial effort to measure the absolute ^{140}Ce total cross section employed a neutron producing target fabricated from tantalum (Ta). It became clear from early measurements that a 110 MeV electron beam with an average current of 55 μA striking this target did not produce neutrons of sufficient intensity above 20 MeV. Therefore, a new neutron-producing target was constructed (see Fig. 2). It consisted of a layer of Ta slightly thicker than one radiation length which was followed by sheets of beryllium (Be). The thickness of the Ta was chosen to maximize neutron production in the Be sheets following the Ta.[6] A comparison of the neutron flux obtained with the Ta and the Ta-Be targets as a function of neutron energy is shown in Fig. 3. This relative flux measurement was made with the neutron detector located at 250 m. The Ta-Be and Ta targets were in the electron beam for equal amounts of time while the machine current was held constant. As can be seen from Fig. 3, the Ta-Be target gave significantly greater neutron intensity between 20 and 50 MeV and, for our purposes, sufficient flux down to several MeV. An important feature of the Ta-Be target was that it produced a less intense gamma flash into the 250-m detector. This helped to reduce the amount of high energy ($E \simeq 60$ MeV) background that must be subtracted from the data. The ^{140}Ce absolute σ_T measurements were made with both neutron-producing targets. All cross section difference measurements were made using the Ta-Be target.

C. Neutron detector

The ^{140}Ce absolute σ_T measurement was begun with a detector which consisted of three separate cylindrical plastic scintillators 12.7×12.7 cm, each viewed by two fast

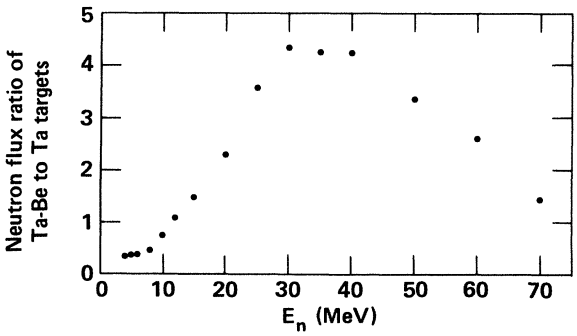

FIG. 3. The relative neutron flux as a function of energy produced by the Ta-Be and Ta targets. The maximum beam intensity for this measurement was determined by the intensity of the gamma flash our detector could accept at 250 m.

12.7 cm diam phototubes operating in a coincidence mode. In order to increase detection efficiency of high-energy neutrons, we constructed a new detector consisting of sixteen separate square scintillators $25.4\times25.4\times5.1$ cm thick. Each scintillator was connected via light pipes to two 5.1 cm diam fast phototubes. This detector has great flexibility since each scintillator can be operated independently and the size of the gamma flash response in each scintillator is manageable. A schematic representation of the detector is shown in Fig. 4. The ^{140}Ce σ_T measurement was carried out with both detector systems described above. The cross section difference measurements were made only with the new detector.

Since we were interested in extending these measurements to as high an energy as possible, it was important to reduce the gamma flash which accompanies neutron production. Even with the detector 250 m from the neutron producing target, it was necessary to keep 2.5 cm of Ta in the neutron beam at all times for gamma flash suppression. This was in addition to the considerable gamma flash suppression provided by the samples ($Z\simeq58$) themselves. 60-MeV neutrons reach the detector only 1.7 μsec after the gamma rays and the detector must recover in this time. After experimentation we arrived at a satisfactory tradeoff between gamma flash recovery and neutron intensity, and with the improved neutron target and detector we were able to carry out our measurements to a maximum neutron energy of 60 MeV.

D. Data acquisition

The data needed to determine the total cross sections for each sample in this experiment are the number of events produced by the neutron beam in the detector as a function of neutron energy. The energy of these events was obtained using the time-of-flight technique. Signals from the neutron detector were used to stop a time digitizer started with a signal generated by the electron beam pulse from the accelerator. The detector signals were gated off during the gamma flash to prevent the digitizer from being disabled for every beam burst. The quartz crystal oscillator of this digitizer maintained a very stable time interval from which the flight times were determined. These flight times were used by the data acquisition computer to sort each event into its appropriate flight time channel. The flight time spectra were divided into channels of varying time width to reduce the amount of storage required for each sample. At high energies these channels were 4 nsec wide while at the lowest energies 64 nsec-wide channels were used.

Spectra for each sample were recorded on a large magnetic disk at the end of each cycling of the samples. The data acquisition system automatically controlled the cycling of samples into the neutron beam when a predetermined number of events was detected by the monitor detector. This detector was gated to respond to the neutron energy range of interest. When the samples were cycled, the monitor information for the sample was also recorded on a magnetic disk.

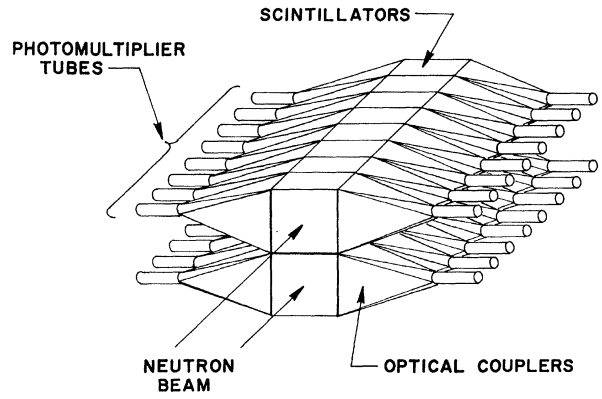

FIG. 4. A schematic view of the neutron detector located 250 m from the neutron-producing target. The detector consists of 16 independent square plastic scintillators each viewed by two photomultiplyer tubes operating in a coincidence mode.

III. CROSS SECTION MEASUREMENTS

A. Absolute neutron total cross section of ^{140}Ce

The main purpose of making an accurate measurement of the ^{140}Ce total cross section was to obtain high quality data over the energy range of interest to which an optical model fit could be made. Since, as described below, the difference cross sections were all carried out with respect to ^{140}Ce, changes of the parameters of this optical potential enabled us to learn about differences between neighboring nuclei.

The ^{140}Ce sample, which contained 99.7% ^{140}Ce, was in the chemical form CeO_2. The CeO_2 was placed in a cylindrical container with a diameter of 15 mm, and the ^{140}Ce had a net thickness of $n=0.1787$ atoms/b (see Table I). The sample-in/sample-out technique was used to measure the cross section. The sample out was a cylinder of H_2O with the number of oxygen atoms matched to that of the ^{140}Ce sample. The samples were cycled in and out of the beam every 10 min. The neutron beam was collimated down to 10 mm at the samples which were placed about 7 m from the neutron-producing target. The effect of hydrogen on the measured transmission was unfolded analytically. This was accomplished by using the effec-

TABLE I. The number of atoms/b, n, for each element in our samples.

Sample	Element	n (atoms/b)
$^{140}CeO_2$	^{140}Ce	0.1787
$^{140}CeO_2$	^{142}Ce	0.000466
$^{140}CeO_2$	O	0.3583
$^{142}CeO_2$	^{140}Ce	0.0130
$^{142}CeO_2$	^{142}Ce	0.1662
$^{142}CeO_2$	O	0.3584
Ce	^{140}Ce	0.2964
Ce	^{142}Ce	0.0369
Pr	^{141}Pr	0.3334
La	^{139}La	0.3331

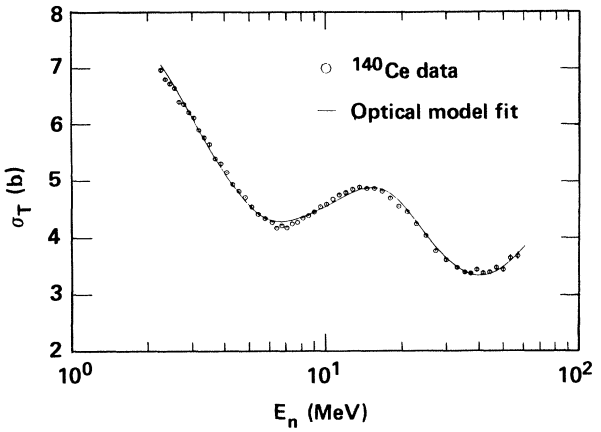

FIG. 5. The measured ^{140}Ce total neutron cross section as a function of energy. Statistical errors for this data are less than the size of the plotting symbol. The solid line is our optical model fit to the data.

tive range expansion of the n,p cross section below 25 MeV prescribed by Lomon and Wilson[7] and Binstock's parametrization[8] above 25 MeV.

The uncertainty, $\delta\sigma_T$, in our ^{140}Ce σ_T measurement is dominanted at low energies by the uncertainty in the n,p cross section and at high energies by background subtraction. The uncertainties due to normalization, background subtraction, and $\sigma_{n,p}$ corrections contributed a 1.5–2% fractional uncertainty, $\delta\sigma_T/\sigma_T$, over the energy range of the measurement. Figure 5 shows σ_T vs neutron energy for ^{140}Ce. As discussed above, the cross section exhibits maxima and minima as a function of energy. The smooth curve through the data is the result of an optical model calculation discussed below.

B. Cross section difference measurements

The transmission ratio (and hence the cross section difference) of neighboring nuclei can be measured much more accurately than absolute cross sections. The major uncertainties in these measurements are the normalization of sample-in and -out runs and the determination of the number of atoms of a given type in the sample. Statistics are also an important consideration. For example, if the cross section difference is 100 mb and a statistical precision of ± 10 mb is desired, it is necessary to collect about 1 000 000 neutron counts in *both* sample-in and -out runs for just *one* data point. If certain conditions are satisfied, background subtractions play essentially no role in this kind of measurement. The reason for this follows from the expression for the transmission ratio which is given by

$$T_R=(C_1-B_1)/(C_2-B_2)\ ,$$

where C and B represent the counts and backgrounds of the samples. If $B/C \ll 1$, then

$$T_R=C_1/C_2[1-(B_1/C_1-B_2/C_2)]\ .$$

For samples with the same number of nuclei but whose nuclei differ by one or two nucleons, $B_1/C_1=B_2/C_2$ to a high degree, and consequently making or not making background corrections alters T_R by an insignificant amount. Lastly, we note that for a given error in the experimental transmission, cross section difference errors are reduced by using thicker samples. Even with our tight collimation we used no less than about 70 g of the separated isotopes ^{140}Ce and ^{142}Ce. The quantities of separated isotopes available ultimately limit the number of nuclei for which this kind of measurement can be carried out with precision.

The main source of error in determining the number of atoms/b (n) of our samples was caused by uncertainties in the geometry of our samples. We determined the fractional uncertainty $\delta n/n$ to be 3.3×10^{-4} for each constituent of the sample. We initially carried out measurements on the ^{139}La$-^{140}$Ce and ^{141}Pr$-^{140}$Ce differences using praseodymium and lanthanum oxides. Unfortunately, these oxides are extremely hydroscopic and easily absorb significant amounts of water in the time required to prepare a sample. Our attempts to determine the H_2O contamination by heating and weighing techniques were not successful. Therefore, we used cylindrical metal samples of Ce, La, and Pr with masses known to five places and a common diameter of 1.4910 ± 0.0005 cm. These metal samples were placed in identical stainless steel holders which were backfilled with argon to prevent oxidation. A spectroscopic analysis of the metal samples indicated no significant impurities. While oxygen contamination can be a problem, the cross section difference data are sensitive to oxygen contamination because the oxygen total cross section has a great deal of structure up to about 8 MeV. The absence of this structure in our difference cross section data indicated that oxygen contamination was not important. The thicknesses of our oxide and metal samples are listed in Table I. Only the measurements of the ^{139}La$-^{140}$Ce and ^{141}Pr$-^{140}$Ce differences performed with the metal samples are reported below.

C. Difference cross section data analysis

The analysis of all the difference data (^{139}La$-^{140}$Ce, ^{141}Pr$-^{140}$Ce, and ^{142}Ce$-^{140}$Ce) is similar, so we confine our discussion to the case in which $^{140}CeO_2$ and $^{142}CeO_2$ were the sample-in and -out, respectively. After dead-time corrections and background subtractions are made the experimental transmission ratio is related to the cross sections by

$$T_R=\exp\left(-\sum n_i^{140}\sigma_i+\sum n_i^{142}\sigma_i\right)\ ,$$

where the sums are over all the constituents of the samples. The total cross section difference $\sigma_T^{142}-\sigma_T^{140}$ can be expressed as:

$$\sigma_T^{142}-\sigma_T^{140}=\frac{1}{n_{142}^{142}}\ln(T_R)+\frac{(n_{ox}^{140}-n_{ox}^{142})\sigma_T^{ox}}{n_{142}^{142}}-\frac{[(n_{142}^{142}+n_{140}^{142})-(n_{140}^{140}+n_{142}^{140})]}{n_{142}^{142}}\sigma_T^{140}+\frac{n_{142}^{140}}{n_{142}^{142}}(\sigma_T^{142}-\sigma_T^{140})\ , \quad (1)$$

where the symbol n_{ox}^{140} means the number of oxygen

atoms/b contained in the $^{140}CeO_2$ sample, etc. Equation (1) indicates the corrections that must be made to the dominant $1/n[\ln(T_R)]$ term which gives $\Delta\sigma_T$ to first order. The second, third, and fourth terms of Eq. (1) contributed, in this case, a total of -1.5 mb. For the other samples the "extra" terms contributed as much as 15 mb. The uncertainty $\delta(\Delta\sigma_T)$ of $\Delta\sigma_T$ receives a contribution from each term of Eq. (1). The $1/n[\ln(T_R)]$ term gives the largest uncertainty, which is ± 10 mb. This error arises from the uncertainty in normalization of the sample-in and -out runs. It was determined by comparing different sets of data. The contributions to $\delta(\Delta\sigma_T)$ from the second and third terms of Eq. (1) arose mainly from the $\delta n/n$ of the n values and were ± 5 and ± 3 mb, respectively. The last term was insignificant. Thus the combined absolute uncertainty of our meaured $\Delta\sigma_T$ is ± 12 mb.

For reasons discussed above, background subtractions do not play a significant role in the analysis as long as $B/C \ll 1$. Three different types of backgrounds were subtracted from the data; ambient, high, and low energy backgrounds. During each accelerator pulse our detection system was enabled well before the electron beam struck the neutron producing target. Thus our TOF spectrum consisted of pregamma flash counts in addition to neutron counts subsequent to the gamma flash. The pregamma flash counts were constant in time and represented our ambient background under operating conditions. Figure 6 shows a typical sample spectrum at the high energy end after ambient background and dead-time corrections were made. The tail of the gamma flash was found to follow an $A\exp(-t/\tau)$ decay with τ typically equal to 470 nsec. This background curve was extrapolated, as shown in Fig. 6, into the region where the neutron counts exist. At 60 MeV the condition $B/C \ll 1$ is reasonably satisfied and it was found that varying A and τ within reasonable limits did not effect the cross section difference. In the low energy region the discriminator setting reduced the neutron counts to zero at ~ 1 MeV, leaving residual counts which were above our ambient background. This residual low energy background was extrapolated to higher energies, and the energy at which the cross section difference became insensitive to the method of extrapolation determined our lowest energy data point.

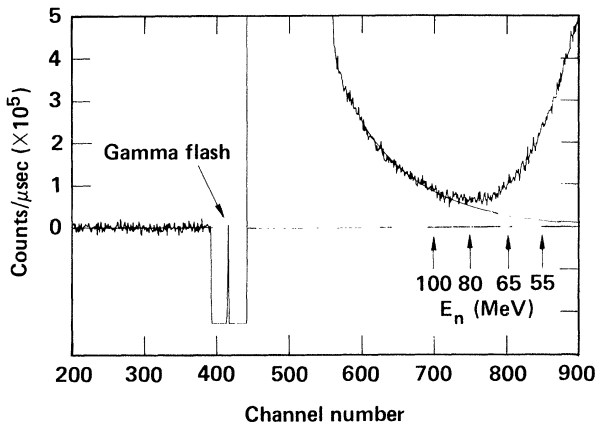

FIG. 6. A typical neutron time-of-flight spectrum at the highest energies after dead time corrections and ambient background subtractions have been made. The data acquisition system was enabled approximately 1.6 μsec before the gamma flash to allow a measurement of the ambient background. It was disabled for approximately 200 nsec before and after the arrival of the gamma flash at the neutron detector. The spike in channel 415 marks the actual gamma flash channel from which the true time=0 channel can be calculated. A least-squares fit to the gamma flash tail between channels 575 and 675 with an exponential decay function is shown superimposed on the time-of-flight spectrum. It was used to correct the highest energy data.

Analyses similar to that described above were carried out for the $^{139}La-^{140}Ce$ and $^{141}Pr-^{140}Ce$ data. Tables II–IV list the cross section difference, $\Delta\sigma_T$, vs neutron energy for the different nuclei, and the data are plotted in Figs. 7–9. For all the nuclei $\Delta\sigma_T$ exhibits oscillations as a function of energy. Since the positions of the maxima and minima of σ_T vs E shown in Fig. 5 depend on the radius of the potential, adding or subtracting nucleons shifts the pattern to higher or lower energies. In addition, adding or subtracting nucleons also raises or lowers the absolute value of the cross section. From these shifts it is possible to understand, qualitatively, the oscillatory behavior of $\Delta\sigma_T$ vs E.

IV. OPTICAL MODEL CALCULATIONS

Since all the nuclei studied (except ^{142}Ce) have a closed neutron shell ($N=82$), it is appropriate to perform optical model calculations using a spherical optical potential which includes spin-orbit coupling. Below approximately 15–20 MeV there exist many precision measurements of the neutron total and elastic differential cross sections over a range of spherical nuclei. Modern phenomenological optical potentials, e.g., the Ohio University global neutron potential of Rapaport *et al.*,[9] use a Woods-Saxon shape for the real part of the potential and both surface

TABLE II. $^{139}La-^{140}Ce$ experimental neutron total cross section differences and their statistical uncertainty as a function of neutron energy.

E (MeV)	$\Delta\sigma_T=\sigma_T^{139}-\sigma_T^{140}$ (mb)	$\delta(\Delta\sigma_T)$ (mb)
2.60	−41.3	13.4
3.10	−102.2	8.5
3.77	−104.1	5.8
4.68	−46.0	2.6
5.84	−21.6	1.9
6.96	−4.9	1.9
8.03	−3.1	2.1
9.39	+19.2	2.1
11.1	+19.8	2.0
13.4	+1.8	2.5
16.4	−26.2	2.4
20.6	−46.1	2.6
26.8	−59.3	2.5
33.7	−49.9	4.4
40.4	−25.6	6.1
48.4	−36.6	9.3
59.2	−17.6	21.5

TABLE III. $^{141}Pr-^{140}Ce$ experimental neutron total cross section differences and their statistical uncertainty as a function of neutron energy.

E (MeV)	$\Delta\sigma_T=\sigma_T^{141}-\sigma_T^{140}$ (mb)	$\delta(\Delta\sigma_T)$ (mb)
3.09	126.4	9.3
3.63	144.0	6.1
4.32	127.7	4.1
5.23	80.6	2.8
6.18	42.9	2.3
7.00	33.1	2.6
7.89	14.0	2.2
8.96	8.5	2.0
10.3	−0.1	2.2
11.9	8.5	2.8
13.9	19.3	2.9
16.6	38.5	3.2
20.0	56.5	2.7
24.7	64.2	2.4
30.2	63.1	3.2
35.3	46.8	5.3
40.5	41.7	5.9
47.1	29.6	8.2
55.4	33.7	16.8

and volume absorption terms in the imaginary part of the potential. At these lower energies the surface absorption term dominates and these potentials are quite successful in fitting a wide range of cross section data. At higher energies, where accurate neutron total cross section and angular distribution data are scarce or nonexistent, proton scattering data seem to indicate that volume absorption dominates surface absorption in the imaginary part of the potential.[10] As a guide to phenomenological parameter fitting, the real and imaginary volume integrals, described below, are important because they are not sensitive to particular forms of the potential used to fit the data. Microscopic folding models,[11] in which a two-body interaction is convoluted with a matter distribution, lend some guidance on the shape and magnitude of these volume integrals at the higher energies.

TABLE IV. $^{142}Ce-^{140}Ce$ experimental neutron total cross section differences and their statistical uncertainty as a function of neutron energy.

E (MeV)	$\Delta\sigma_T=\sigma_T^{142}-\sigma_T^{140}$ (mb)	$\delta(\Delta\sigma_T)$ (mb)
2.98	12.7	9.5
3.61	43.8	9.5
4.45	74.3	5.4
5.63	92.0	4.3
6.75	92.7	5.4
7.78	85.2	5.7
9.07	76.4	5.8
10.7	48.8	6.5
12.8	39.6	7.3
15.7	54.3	7.9
19.6	45.8	8.0
25.2	91.0	8.2
32.7	83.7	11.0
38.9	80.6	16.6
46.5	50.2	23.0
56.5	30.6	37.9

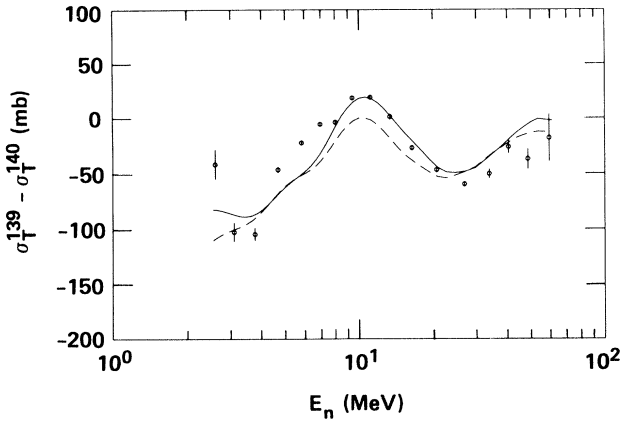

FIG. 7. The total cross section difference of $^{139}La-^{140}Ce$ as a function of neutron energy. Only statistical errors are plotted for the total cross section difference. The dashed curve was calculated using the ^{140}Ce value in the $(N-Z)/A$ terms in the potential and varying only the geometrical parameters R and A. The solid curve, which gives an improved fit, was calculated by letting the $(N-Z)/A$ terms assume the ^{139}La value and by changing R from 6.52 (the ^{140}Ce value) to 6.50 fm.

Several forms of phenomenological optical potentials were used in analyzing the total cross section data of this measurement (see below and the appendices). Included was the Ohio University global neutron potential, which was modified at high energies in a reasonable way to fit the shape and magnitude of our total cross section data. However, all of the potentials used suffer inadequacies of one form or another at high energies. Each of the potentials yielded a different shape and magnitude for the imaginary volume integral and therefore the reaction cross section. They also predict different shapes for elastic an-

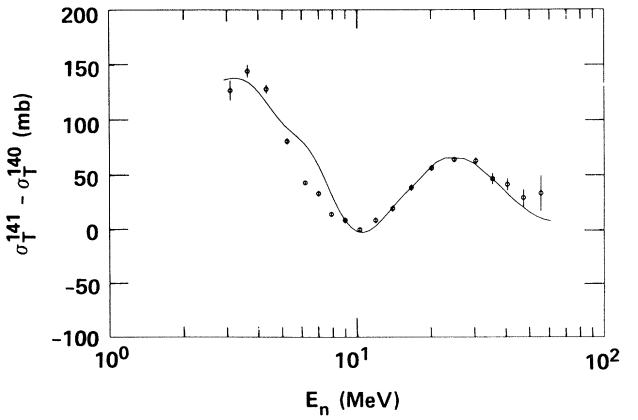

FIG. 8. The total cross section difference of $^{141}Pr-^{140}Ce$ as a function of neutron energy. The solid line is an optical model calculation generated by changing R from 6.52 (the ^{140}Ce value) to 6.54 fm and a from 0.70 (the ^{140}Ce value) to 0.71 fm.

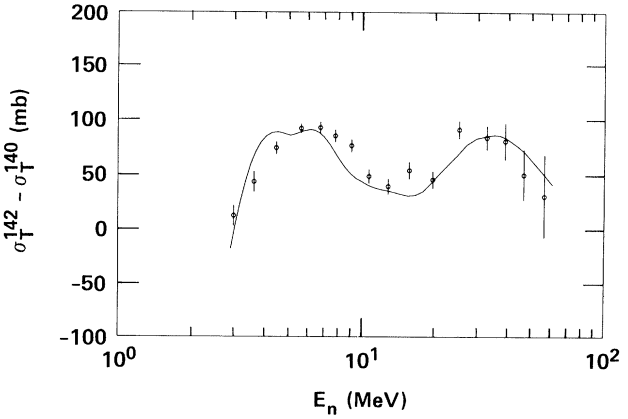

FIG. 9. The ^{142}Ce$-^{140}$Ce total cross section difference as a function of energy. Small changes in the geometrical parameters of the optical potential could not reproduce the general trend of the data. It was also necessary to increase the strength of the imaginary part of the potential to generate the solid line shown.

gular distributions at high energies where no data yet exist to provide a basis for selection. However, each of the potentials fits our total cross section data well over the wide energy range of the experiment. While the neutron total cross section is an important constraint in determining optical model parameters, these data by themselves are not sufficient to determine unique parameters. Important experimental data needed at this time to pinpoint adequately the deficiencies of these optical potentials are neutron angular distributions, especially at larger angles, on spherical nuclei in the 40–60 MeV neutron energy range.

Our interest is not in determining an optical potential *per se*, but rather using an optical model analysis to explore differences between neighboring nuclei. Thus the primary concern is that the conclusions of this work should be relatively insensitive to the particular optical model employed.

A. Total cross section calculations

We have investigated three optical model potentials and have chosen the functional form used by Dukarevich, Dyumin, and Kaminker[12] (hereafter referred to as DDK) to carry out the most detailed fitting of our total absolute and difference cross section data. As can be seen below and in the appendices, our general conclusions appear to be independent of the explicit form of the potential. The functional form of the DDK potential contains a surface absorption term only in the imaginary part, but, nevertheless, fits the total and difference cross sections well, reproduces the measured reaction and neutron angular distributions over a wide range of nuclei and energies, and, because of its form, has a smaller number of parameters.

DDK carried out a series of neutron total cross section measurements at 14.2 MeV on a large number of isotopes ranging from ^{58}Ni to ^{209}Bi. (They did not examine the mass 140 region.) They analyzed their 14.2 MeV data with a potential of the following form:

$$U(r)=Vf(r)+iWg(r)+V_{so}\left[\frac{\hbar}{m_\pi c}\right]^2\frac{1}{r}\left|\frac{df}{dr}\right|\vec{\sigma}\cdot\vec{l}\ , \quad (2a)$$

$$f(r)=\left[1+e^{\frac{(r-R)}{a}}\right]^{-1}, \quad (2b)$$

$$g(r)=e^{-\left[\frac{r-R}{b}\right]^2}. \quad (2c)$$

In order to fit their data they found it necessary to introduce an $(N-Z)/A$ dependence in the real and imaginary strengths of the potential. This dependence is expected on theoretical grounds.[13] The analysis of DDK yielded the following parameters:

$$V=-45.5+17(N-Z)/A\ , \quad (3a)$$

$$W=-14.5+26(N-Z)/A\ , \quad (3b)$$

$$V_{so}=-8.3;\ b=1.0\ ,$$
$$R=r_0A^{1/3};\ r_0=1.26;\ a=0.70\ , \quad (3c)$$

where all strengths are in MeV and lengths are in fm.

We have performed optical model calculations with the code OPTICAL (Ref. 14) using the same *functional form* of the potential as used by DDK. We set $V_{so}=-8.3$ and $b=1.0$ but allowed all other parameters to be unconstrained. A search for a good fit to the ^{140}Ce total cross section data between 2.5 and 60 MeV yielded the following parameters:

$$V=-47.0+0.30E,\ E<25\ \text{MeV}\ ,$$
$$V=-43.25+0.15E,\ E\geq 25\ \text{MeV}\ ; \quad (4a)$$

$$W=-3.0+1.4E,\ E<5\ \text{MeV}\ ,$$
$$W=-12.0(1-e^{-E/2.3}),\ E\geq 5\ \text{MeV}\ ; \quad (4b)$$

$$R=6.52;\ a=0.70;\ b=1.0;\ V_{so}=-8.3\ , \quad (4c)$$

where E is the incident neutron energy. The geometrical parameters, $R=6.52$ and $a=0.70$, that we found are almost identical to the values of 6.54 and 0.70 suggested by DDK for $A=140$. In addition, at 14.2 MeV our strength parameters, $V=-42.74$ and $W=-11.98$, agree well with the values of -42.59 and -10.04 implied by DDK for ^{140}Ce, particularly for the real potential strength. It was not obvious *a priori* that starting from the same functional form of the potential our fit on a single nucleus covering a large energy range should result in parameters for ^{140}Ce which agree so well at 14.2 MeV with DDK's implied values for this nucleus.

Since our parameters [Eqs. (4a)–(4c)] are in good agreement with those of DDK at 14.2 MeV, we can use our fit of the ^{140}Ce data as a guide to the energy dependence of the potential given by Eqs. (2) and (3). In order to introduce an $(N-Z)/A$ dependence in the real potential strength, which also gives a *total* energy dependence of the real part given by Eq. (4), we assumed a real potential strength of the form

$$V=-V_0+a_1E+(V_1-a_2E)(N-Z)/A\ , \quad (5)$$

and required that the ratio of the isospin to central term be independent of energy, i.e.,

$$(V_1-a_2E)\left[\frac{N-Z}{A}\right]\Big/(-V_0+a_1E)=\text{constant} . \quad (6)$$

A constraint like Eq. (6) was needed to reduce the number of free parameters. With this constraint, choosing $V_1=17$ MeV and requiring V to have the energy dependence given by Eq. (4), we obtained the following expressions for the real part of the potential when the $(N-Z)/A$ term is included:

$$V=-49.9+0.32E+(17.0-0.111E)(N-Z)/A ,$$
$$E<25 \text{ MeV} ; \quad (7a)$$
$$V=-45.88+0.159E+(15.58-0.054E)(N-Z)/A ,$$
$$E\geq 25 \text{ MeV} .$$

For the imaginary part of the potential a similar procedure was followed. The central strength of the imaginary potential has an essentially constant value of -16.2 MeV for neutron energies from 10 to 60 MeV. We used the constraint that above 10 MeV the ratio of the central to isospin term of the imaginary part of the potential be constant. This translates into an energy independent $(N-Z)/A$ term whose strength was chosen to be 26 MeV as was found by DDK at 14.2 MeV. Below 10 MeV the $(N-Z)/A$ term was taken to be constant even though the central strength of the imaginary part of the potential did vary with energy. The expressions used for the imaginary part of the potential were the following:

$$W=-7.456-1.4E+26(N-Z)/A, \quad E<5 \text{ MeV} , \quad (7b)$$
$$W=-16.32(1-e^{-E/2.3})+26(N-Z)/A, \quad E\geq 5 \text{ MeV} .$$

With $V_{so}=-8.3$, $b=1.0$, $a=0.70$, $R=6.52$, and V and W given by Eqs. (7a) and (7b), we obtain the fit for ^{140}Ce shown in Fig. 5. The calculated cross section is in good agreement with the data over the full energy range of the measurement. An interesting feature of the real part of this potential and the potential given in Appendix A is the energy dependence we found necessary to use in order to fit the data. Equation (7a) [or equivalently (4a)] indicates that the potential strength decreases with energy but that the rate of decrease diminishes as the neutron energy increases. A qualitatively similar energy behavior for a local potential was deduced by Engelbrecht and Fiedeldey[15] who reduced a nonlocal potential to its equivalent local form.

Since the potential which includes only surface absorption possesses fewer parameters, it was more convenient to use and thus formed the basis of our optical model analysis. The potential represented by Eqs. (7a) and (7b) reproduces reasonably well experimental elastic neutron angular distributions over a wide range of mass and energy. Typical fits to angular distribution data[16] are shown in Fig. 10. We do not expect our fits to the data to be of the same quality as those potentials whose parameters are determined by angular distribution data, e.g., the Ohio potential. However, it is interesting to note that fitting neutron total cross section data for a range of nuclei (DDK) and energy (this work) leads to an optical potential which gives a reasonable picture of angular distributions.

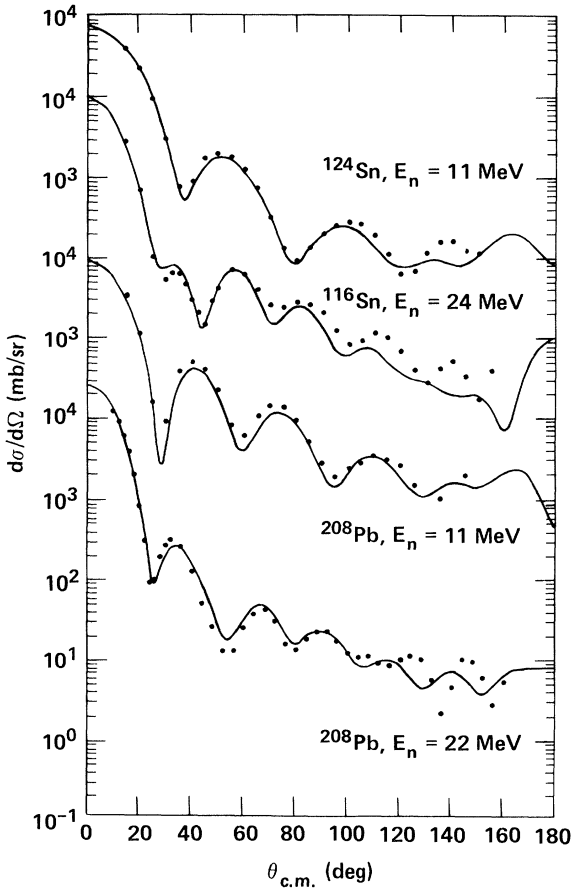

FIG. 10. Experimental elastic neutron angular distributions from Ref. 16 for ^{124}Sn at $E_n=11$ MeV and ^{116}Sn at $E_n=24$ MeV, as well as for ^{208}Pb at $E_n=11$ and 22 MeV, respectively. The solid lines represent our optical model calculations as described in the text.

The volume integral,

$$J_v/A=-\int V(r)d\vec{r}/A ,$$

where $V(r)$ is the real part of the potential, is not sensitive to the particular form of the potential used to fit data. The solid curve of Fig. 11 represents J_v/A as a function of neutron energy for our potential [Eqs. (7a) and (7b)] and geometrical parameters given above. Since the potential we have used is local and R and a are not energy dependent, the energy variation of J_v/A just reflects that of the real potential strength. The three curves of Fig. 11 represent J_v/A for the potentials that were used to analyze the data (see also the appendices). Kailas and Gupta[17] have calculated volume integrals for neutron optical potentials used to fit neutron data over a large range of A values at an average neutron energy of 5 MeV. For $A=140$, their results imply that J_v/A should be 418 MeV fm^3. At 5 MeV our value of J_v/A as shown in Fig. 11 (solid curve) is also 418 MeV fm^3. We have further compared our J_v/A values with those of Rapaport

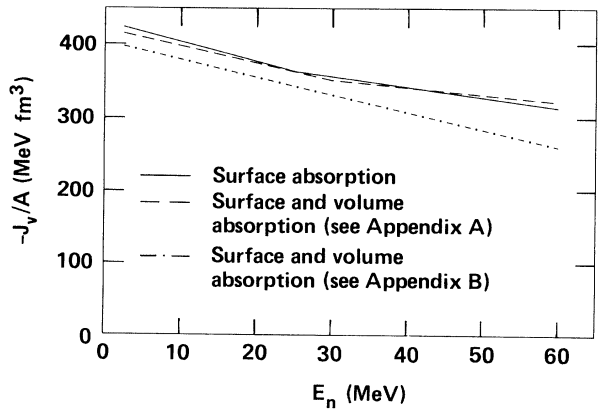

FIG. 11. The energy dependence of J_v/A as determined by our optical model fit to the ^{140}Ce total cross section data. The solid and dashed curves represent the behavior of J_v/A using a potential whose imaginary part contained only surface absorption and one containing surface plus volume absorption, respectively (Appendix A). The dotted-dashed curve was calculated using the Ohio University potential discussed in Appendix B.

et al.[18] who carried out neutron angular distribution measurements on ^{100}Mo which has an $(N-Z)/A$ value similar to that of ^{140}Ce. Over the energy range 7–26 MeV our J_v/A values are, on the average, 6% larger than their ^{100}Mo J_v/A values, which is a reasonable agreement.

B. Optical model fit of cross section differences

Using the optical potential defined by Eqs. (2) and (7) we calculated the neutron total cross section differences and compared the predicted values with the experimental values for the nuclei ^{139}La, ^{141}Pr, and ^{142}Ce. For ^{139}La an attempt was first made to fit the $\sigma_T^{139}-\sigma_T^{140}$ data by changing only the geometrical parameters of the potential from those determined for ^{140}Ce. The $(N-Z)/A$ terms in the real and imaginary parts of the potential were held fixed to the ^{140}Ce value. The fit obtained in this fashion is shown by the dashed curve in Fig. 7. By letting the $(N-Z)/A$ term assume the value for ^{139}La and searching on the geometrical parameters, the fit represented by the solid line was found. The solid line is in better agreement with the data than the dotted line and implies that the asymmetry terms in the potential are necessary as expected. Since the data are fit over a large energy range it also suggests that our assumption concerning the energy independence of the ratio of the isospin to the central part of the real potential is not unreasonable, at least up to 60 MeV.

In summary, an acceptable fit to the $\sigma_T^{139}-\sigma_T^{140}$ cross section difference was obtained by including the $(N-Z)/A$ term in the potential and by decreasing R in the Woods-Saxon form factor from the ^{140}Ce value of 6.52 to 6.50. The diffuseness of the real and imaginary parts of the potential remained unchanged.

For ^{141}Pr an attempt was also made to fit the $\sigma_T^{141}-\sigma_T^{140}$ data by changing only geometrical parameters of the potential, as was described above for ^{139}La. In this case too we found that including the $(N-Z)/A$ terms in the potential improved the fit to the data. The $\sigma_T^{141}-\sigma_T^{140}$ data are plotted in Fig. 8 along with the optical model calculation, which is represented by the solid line. The fit to the data is quite satisfactory and was achieved by increasing R from 6.52 (the ^{140}Ce value) to 6.54 and the diffuseness from 0.70 (the ^{140}Ce value) to 0.71. It is remarkable that for the $\sigma_T^{139}-\sigma_T^{140}$ and $\sigma_T^{141}-\sigma_T^{140}$ data the optical model calculations fit the data as well as they do with such minor changes of the parameters.

We note that the oscillations in the difference data are reproduced quite naturally without invoking nuclear deformations. Shamu *et al.*[19] have measured neutron total cross section differences for Nd and Sm isotopes and were able to deduce deformation parameters from their coupled-channel optical model analysis. Although nuclear deformations can play an important role in producing oscillations in the difference data for nonspherical nuclei, as these authors emphasized, we note that our results indicate that oscillations of $\Delta\sigma_T$ also occur for nuclei which can be thought of as being spherical.

In the case of ^{142}Ce we were not able to fit the $\sigma_T^{142}-\sigma_T^{140}$ data by making minor adjustments in just one or two parameters as was done for ^{139}La and ^{141}Pr. In addition to changing R and a to 6.54 and 0.72, it was also necessary to increase the strength of the imaginary part of the potential and introduce a slight energy dependence in the width b of the form factor $g(r)$ of Eq. (2). The expressions used for W and b are the following:

$$W=-10.88-0.715E+20(N-Z)/A,\quad E<5\text{ MeV},\tag{8a}$$

$$W=-16.32(1-e^{-E/2.3})+20(N-Z)/A,\quad E\geq\text{ MeV};$$

$$b=0.97+0.05(E-3)/7,\quad E<10\text{ MeV},\tag{8b}$$

$$b=1.02,\quad E\geq 10\text{ MeV}.$$

The fit to the data we obtained with these changes is shown by the solid line of Fig. 9. The calculated $\Delta\sigma_T$ reproduces the data reasonably well. In essence the changes required from the ^{140}Ce parameters indicate greater diffuseness and an increased reaction cross section for ^{142}Ce. Thus we conclude that whereas ^{139}La, ^{140}Ce, and ^{141}Pr are similar, a change of a more abrupt nature occurs by adding two neutrons to ^{140}Ce than when a proton is added or subtracted from ^{140}Ce. Part of the increased diffuseness may be explained by the fact that the two additional neutrons enter a new major shell and consequently are more weakly bound. The tails of these neutron wave functions would die off less rapidly with distance. If the ^{142}Ce nucleus has a nonspherical shape with respect to ^{140}Ce, this would also manifest itself as an increased diffuseness in a spherical optical model calculation.

C. Optical model and charge distribution parameters

Table V lists the geometrical parameters of the real part of the potential along with $\langle r^2\rangle$ values for the four nuclei studied. $\langle r^2\rangle$ is defined by

$$\langle r^2\rangle=\int r^2V(r)d\vec{r}/\int V(r)d\vec{r},\tag{9}$$

TABLE V. Geometrical optical model parameters for the real part of the potential determined for the four nuclei studied along with $\langle r^2 \rangle$ values calculated using our optical model parameters and parameters derived from muonic x-ray data.

Nucleus	R (fm)	a (fm)	$\langle r^2 \rangle_0$ (fm^2)	$\langle r^2 \rangle_q$ (fm^2)
^{139}La	6.50	0.70	32.12	23.57
^{140}Ce	6.52	0.70	32.28	23.79
^{141}Pr	6.54	0.71	32.63	23.94
^{142}Ce	6.54	0.72	32.83	24.07

where $V(r)$ is the real part of the potential. For our potential $V(r)$ can be replaced by $f(r)$ which is a measure of the "shape" of the neutron-nucleus potential. In the fourth column of Table V we list $\langle r^2 \rangle_0$ values determined from our optical model analysis and in the last column the $\langle r^2 \rangle_q$ values listed were determined from muonic x-ray data[20] with the $V(r)$ of Eq. (9) replaced by a Woods-Saxon shaped charged distribution. The $\langle r^2 \rangle_q$ values determined from the muonic data included the size of the proton. Table VI lists values of $\delta(r^2) = {}^A\langle r^2 \rangle - {}^{140}\langle r^2 \rangle$ for the nuclei whose total cross section differences were measured. The second and third columns give the optical model and muonic x-ray data values, respectively. The values of $\delta(r^2)$ determined through the optical model calculations do not appear to be overly sensitive to the potential used to fit the data. For example, as shown in Appendix A, fitting the ^{141}Pr$-^{140}$Ce difference data using a potential which included both surface and volume absorption yielded a value of $\delta(r^2) = 0.28$ fm^2. This is close to the value of 0.35 fm^2 given in Table VI and within the quoted uncertainty of 0.14 fm^2 which results from varying the optical model parameters to fit the data within the ± 12 mb systematic uncertainty of $\Delta\sigma_T$. Another example of the relative insensitivity of $\delta(r^2)$ to the form of the potential is given in Appendix B where the Ohio global potential was modified to fit our ^{140}Ce total cross section data and then used to fit the ^{139}La$-^{140}$Ce difference data. This potential yielded the value of -0.11 fm^2 which is close to the value of -0.16 fm^2 given in Table VI.

If the charge and matter distributions are assumed to have the same $\langle r^2 \rangle$ values, then, within the context of a simple folding model (for the real part of the potential) in which a two-body interaction is convoluted with a matter distribution, the relationship

$$\langle r^2 \rangle_0 = \langle r^2 \rangle_q + \langle r^2 \rangle_{\mathrm{TB}}$$

TABLE VI. $\delta\langle r^2 \rangle$ values determined from our optical model parameters and from parameters determined by muonic x-ray data.

Nuclei	$\delta(r^2)_0$ (fm^2)	$\delta(r^2)_q$ (fm^2)
^{139}La$-^{140}$Ce	-0.16 ± 0.14	-0.21
^{141}Pr$-^{140}$Ce	0.35 ± 0.14	0.15
^{142}Ce$-^{140}$Ce	0.55 ± 0.14	0.28

is expected to apply. For this simple model the optical model and muonic x-ray values of $\delta(r^2)$ should be the same if $\langle r^2 \rangle_m$, the average radius squared of the matter distribution, is the same as $\langle r^2 \rangle_q$, and $\langle r^2 \rangle_{\mathrm{TB}}$ does not vary from nucleus to nucleus. Considering the uncertainties in the cross section difference measurement as well as the slight dependence of $\delta(r^2)$ on the form of the potential used, we conclude that the $\delta(r^2)_0$ values determined for ^{139}La$-^{140}$Ce and ^{141}Pr$-^{140}$Ce are consistent with $\delta(r^2)_q$ calculated for these nuclei using muonic x-ray data. However, for ^{142}Ce$-^{140}$Ce the result that $\delta(r^2)_0 > \delta(r^2)_q$ still holds even after the uncertainties mentioned above are accounted for.

V. SUMMARY

With a moderate electron linac beam intensity and a suitable neutron producing target and detector, we have been able to measure with good precision absolute and relative neutron total cross sections to 60 MeV. The parameters of the potential we have used to analyze the total cross section difference data were determined by total cross section data only, and this potential was found to give a reasonable picture of the behavior of neutron angular distributions as a function of mass number and energy.

Using the optical potential as a diagnostic tool, we found that the effect of adding or subtracting a proton to ^{140}Ce can be explained by making minor and reasonable changes in the geometry of the optical model parameters. Our analysis also indicates that the effect of adding two neutrons to ^{140}Ce cannot be explained in such a simple fashion. The ^{142}Ce$-^{140}$Ce total cross section difference data imply that ^{142}Ce has a larger reaction cross section and is not as spherical as ^{140}Ce.

ACKNOWLEDGMENTS

We would like to thank R. W. Bauer for his constant support and encouragement and C. H. Poppe and F. S. Dietrich for their constructive comments. This work was performed under the auspices of the U.S. Department of Energy by the Lawrence Livermore National Laboratory under Contract No. W-7405-ENG-48.

APPENDIX A

In order to examine the independence of our optical model results to the form of the potential used we have also fit some of our data with a potential which possesses both surface and volume absorption. Using a potential of the form:

$$U(r) = Vf(r) + iW_v f(r) + iW_s f_s(r) + V_{\mathrm{so}} \left[\frac{\hbar}{m_\pi c} \right]^2 \frac{1}{r} \left| \frac{df}{dr} \right| \vec{\sigma} \cdot \vec{l} \,, \tag{A1}$$

$$f(r) = \left[1 + e^{\frac{(r-R)}{a}} \right]^{-1} ,$$

$$f_s(r) = 4e^{\frac{(r-R)}{b}} \left[1 + e^{\frac{(r-R)}{b}} \right]^{-2} ,$$

a search for an acceptable fit to the ^{140}Ce σ_T vs E data led us to the following potential strengths and geometrical parameters:

$$V=-47.0+0.26E,\quad E<30\text{ MeV},$$
$$V=-42.5+0.11E,\quad E>30\text{ MeV};\tag{A2a}$$
$$W_V=0.0,\quad E<7.5\text{ MeV},$$
$$W_V=0.667-0.0889E,\quad 7.5\le E<30\text{ MeV},\tag{A2b}$$
$$W_V=-2.0,\quad E\ge 30\text{ MeV};$$
$$W_S=-3.325-0.67E,\quad E<11.5\text{ MeV},$$
$$W_S=-16.02+0.434E,\quad 11.5\le E<30\text{ MeV},\tag{A2c}$$
$$W_S=-3.0,\quad E\ge 30\text{ MeV};$$
$$V_{so}=-8.3,$$
$$R=6.45,\quad a=0.70,\quad b=0.48.$$

The fit obtained to the ^{140}Ce total cross section with this potential is shown in Fig. 12. The real part of the potential has an energy dependence very similar to that found using the potential which includes only surface absorption.

Following a procedure similar to that which led from Eqs. (4a) to (7a), an $(N-Z)/A$ term was introduced into the real part of the potential which was finally expressed as

$$V=-49.914+0.276E+(17.-0.094E)(N-Z)/A,\quad E<30\text{ MeV},$$
$$V=-45.135+0.1168E+(15.37-0.0398E)(N-Z)/A,\quad E\ge 30\text{ MeV}.\tag{A3}$$

An $(N-Z)/A$ term was not introduced into the imaginary part of the potential. Using Eqs. (A2b), (A2c), and (A3) we examined what changes of R and a would be required to fit the ^{141}Pr$-^{140}$Ce total cross section difference data. By changing R and a from the ^{140}Ce values of 6.45 and 0.70 to 6.473 and 0.705, respectively, we obtained the fit shown in Fig. 13. The value of

$$\delta(r^2)={}^{141}\langle r^2\rangle_0-{}^{140}\langle r^2\rangle_0=0.28\text{ fm}^2$$

calculated with this potential agrees favorably with the value of $\delta(r^2)=0.35$ fm^2 given in Table VI.

APPENDIX B

As a further test of the independence of our conclusions to the particular form of the optical potential used, we have fit some of our data with the Ohio University global neutron potential of Rapaport *et al.*[9] which includes both surface and volume absorption terms. We started with parameter set A (see Ref. 9) which, for the ^{140}Ce total cross section, yielded energy-dependent real and imaginary strengths as follows:

$$V_R=50.30-0.2974E,$$
$$W_V=0.,\tag{B1a}$$
$$W_D=2.086+0.4E$$

for $E\le 15$ MeV, and

$$V_R=50.30-0.2974E,$$
$$W_V=-4.3+0.38E,\tag{B1b}$$
$$W_D=12.22-0.39E$$

for $E\ge 15$ MeV. The expressions for V_R and W_D possess an isospin dependence; the constants appearing in the expressions for V_R and W_D in Eqs. (B1a) and (B1b) reflect the $(N-Z)/A$ values of ^{140}Ce.

The parameters of this potential were deduced from neutron angular distribution data on isotopes ranging from calcium to lead, but not including the mass-140 region, and over a wide range of neutron energies up to 26 MeV. This potential yielded a quite good fit to our ^{140}Ce σ_T data to ~26 MeV but yielded an unsatisfactory fit at the higher energies. The poorer quality fit above 26 MeV

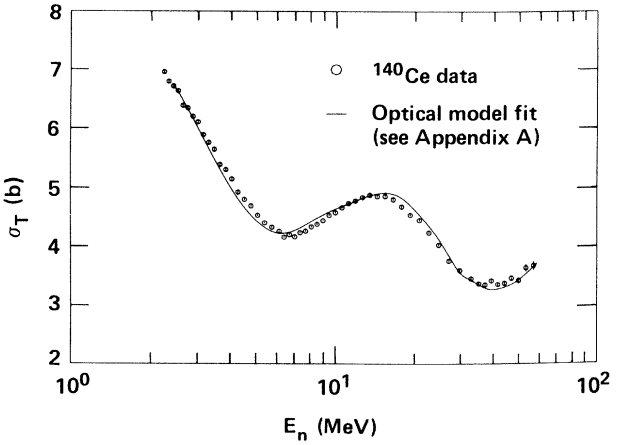

FIG. 12. Optical model fit to the ^{140}Ce total cross section using a potential which contains both surface and volume absorption as described in Appendix A.

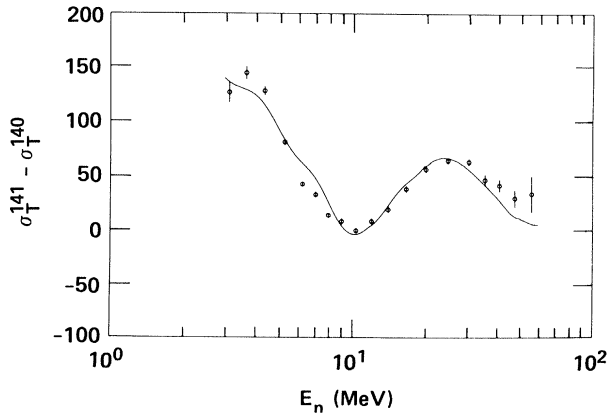

FIG. 13. Optical model fit to the ^{141}Pr$-^{140}$Ce total cross section difference data using a potential which contains surface plus volume absorption. See Appendix A.

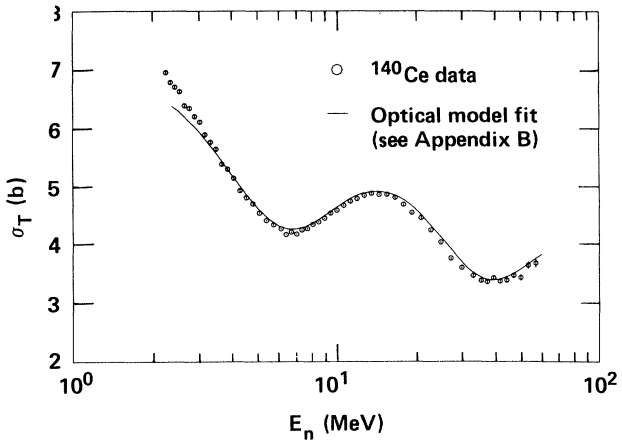

FIG. 14. Optical model fit to the ^{140}Ce total cross section using the Ohio University global potential as described in Appendix B.

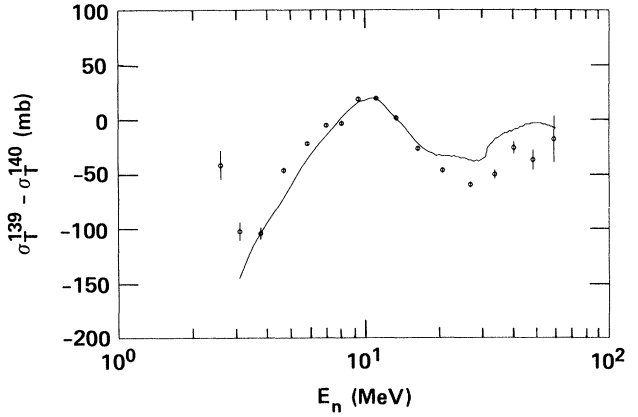

FIG. 15. Optical model fit to the ^{139}La$-^{140}$Ce total cross section difference data using the Ohio University global potential (see Appendix B).

was not surprising because the parameters of this potential were determined by fitting data below 26 MeV. However, with simple modifications to the Ohio University potential above 25 MeV, we obtained the fit shown in Fig. 14. The two modifications to the potential included setting the strength of the volume imaginary part of the potential, W_V, to a constant 5.2 MeV for all energies above 25 MeV and setting the surface imaginary part of the potential, W_D, to zero for all energies above 31 MeV. This is consistent with the values of W_V and W_D at 25 and 31 MeV, respectively, and introduces no discontinuity in the potential. In Fig. 15 we show the comparison of our ^{139}La$-^{140}$Ce total cross section difference data with the cross section difference calculated using the Ohio University global neutron potential modified as described above. No attempt was made to modify the potential to fit the data below 3 MeV in either Fig. 14 or 15.

In calculating the ^{139}La σ_T cross section with this potential, so that the ^{139}La$-^{140}$Ce difference could be computed, the N, Z, and A values of ^{139}La were used [this slightly changed the constant appearing in Eqs. (B1a) and (B1b)] and R was decreased from the ^{140}Ce value of 6.220 to 6.206. No other changes were made. The value of

$$\delta\langle r^2\rangle = {}^{139}\langle r^2\rangle_0 - {}^{140}\langle r^2\rangle_0 = -0.11 \text{ fm}^2$$

calculated with this potential is satisfactorily close to the value of -0.16 fm^2 given in Table VI. The ^{139}La$-^{140}$Ce total cross section difference data is fit almost as well with this potential as with that used in the main body of the work and supports the conclusions drawn with that potential.

[1]D. W. Glasgow and D. G. Foster, Phys. Rev. C 3, 604, (1971); D. G. Foster and D. W. Glasgow, *ibid.* 3, 576 (1971).

[2]G. Haouat, J. Lachkar, Ch. Lagrange, M. T. McEllistrem, Y. Patin, R. E. Shamu, and J. Sigaud, Phys. Rev. C 20, 78 (1979).

[3]J. P. Delaroche, G. Haouat, J. Lachkar, Y. Patin, J. Sigaud, and J. Chardine, Phys. Rev. C 23, 136 (1981).

[4]J. M. Peterson, Phys. Rev. 125, 955 (1962).

[5]H. S. Camarda, Nucl. Instrum. Methods 161, 183 (1979).

[6]M. J. Berger and S. M. Seltzer, Phys. Rev. C 2, 621 (1970).

[7]E. Lomon and R. Wilson, Phys. Rev. C 9, 1329 (1974).

[8]J. Binstock, Phys. Rev. C 10, 19 (1974).

[9]J. Rapaport, V. Kulkarni, and R. W. Finlay, Nucl. Phys. A330, 15 (1979).

[10]F. D. Becchetti and G. W. Greenless, Phys. Rev. 182, 1190 (1969).

[11]J. P. Jeukenne, A. Lejeune, and C. Mahaux, Phys. Rev. C 16, 80 (1977); A. Lejeune, *ibid.* 21, 1107 (1980).

[12]Yu. V. Dukarevich, A. N. Dyumin, and D. M. Kaminker, Nucl. Phys. A92, 433 (1967).

[13]G. R. Satchler, *Isospin in Nuclear Physics,* edited by D. H. Wilkinson (North-Holland, Amsterdam, 1969).

[14]M. E. Smith and H. S. Camarda, Lawrence Livermore National Laboratory Internal Report UCID-18737, 1980.

[15]C. A. Engelbrecht and H. Fiedeldey, Ann. Phys. (N.Y.) 42, 262 (1967).

[16]Data from the National Nuclear Data Center, Brookhaven National Laboratory, from the work of Rapaport *et al.*, Ref. 18.

[17]S. Kailas and S. K. Gupta, Phys. Rev. C 17, 2236 (1978).

[18]J. Rapaport, T. S. Cheema, D. E. Bainum, R. W. Finlay, and J. D. Carlson, Nucl. Phys. A313, 1 (1979).

[19]R. E. Shamu, E. M. Bernstein, D. Blondin, J. J. Ramirez, and G. Rochau, Phys. Lett. 45B, 241 (1973); R. E. Shamu, C. H. Lagrange, E. M. Bernstein, J. J. Ramirez, T. Tamura, and C. Y. Wong, *ibid.* 61B, 29 (1976).

[20]R. Engfer, H. Schneuwly, J. L. Vuilleumier, H. K. Walter, and A. Zehnder, At. Data Nucl. Data Tables 14, 509 (1974).